AAPT PHYSICS EDUCATION | AMERICAN JOURNAL of PHYSICS

Photonic Rutherford scattering: A classical and quantum mechanical analogy in ray and wave optics

Markus Selmke and Frank Cichos

Citation: Am. J. Phys. **81**, 405 (2013); doi: 10.1119/1.4798259
View online: http://dx.doi.org/10.1119/1.4798259
View Table of Contents: http://ajp.aapt.org/resource/1/AJPIAS/v81/i6
Published by the American Association of Physics Teachers

Additional information on Am. J. Phys.

Journal Homepage: http://ajp.aapt.org/
Journal Information: http://ajp.aapt.org/about/about_the_journal
Top downloads: http://ajp.aapt.org/most_downloaded
Information for Authors: http://ajp.dickinson.edu/Contributors/contGenInfo.html

ADVERTISEMENT

Downloaded 20 May 2013 to 139.18.110.156. Redistribution subject to AAPT license or copyright; see http://ajp.aapt.org/authors/copyright_permission

Photonic Rutherford scattering: A classical and quantum mechanical analogy in ray and wave optics

Markus Selmke and Frank Cichos[a),b)]
Molecular Nanophotonics, Institute of Experimental Physics I, Universität Leipzig, 04103 Leipzig, Germany

(Received 9 November 2012; accepted 11 March 2013)

Using Fermat's least-optical-path principle, the family of ray trajectories through a special (but common) type of a gradient refractive index lens $n(r) = n_0 + \Delta nR/r$ is solved analytically. The solution gives a ray equation $r(\phi)$ that is closely related to Rutherford scattering trajectories; we therefore refer to this refraction process as "photonic Rutherford scattering." It is shown that not only do the classical limits correspond but also the wave-mechanical pictures coincide—the time-independent Schrödingier equation and the Helmholtz equation permit the same mapping between the scattering of massive particles and optical scalar waves. Scattering of narrow beams of light finally recovers the classical trajectories. The analysis suggests that photothermal single-particle microscopy measures photonic Rutherford scattering in specific limits and allows for an individual single-scatterer probing. A macroscopic experiment is demonstrated to directly measure the scattering angle to impact parameter relation, which is otherwise accessible only indirectly in Rutherford-scattering experiments.
© *2013 American Association of Physics Teachers.*
[http://dx.doi.org/10.1119/1.4798259]

I. INTRODUCTION

More than 100 years ago in the year 1911, Ernest Rutherford changed our picture of the atom with his famous theory on the scattering of α-particles.[1] In Rutherford scattering, helium nuclei are deflected by the Coulomb potentials of positive gold atom nuclei, as originally shown by Geiger and Mardsen.[2] This work was a milestone in the discovery of the structure of the atom, revealing that most of the mass of an atom is concentrated in a tiny nucleus. Thus, Rutherford scattering is considered in almost every atomic physics course, treated classically to provide the characteristic angular distribution of scattered α particles. While a classical showpiece illustrating Rutherford scattering may be obtained from a paraboloidal hard-wall potential,[3] a direct display of the continuous trajectory, or measuring a single deflection instead of the total cross section, remains difficult.

Here, we present the photonic analog of Rutherford scattering (see Fig. 1). It is given in the geometrical optics approximation (GOA) by the deflection of rays (the classical limit) or, in wave optics, as the scattering of waves by a $1/r$ refractive-index profile. This profile is provided by a point-like heat source in a homogeneous medium. Experimental demonstrations of the effect can be achieved.

The paper is structured as follows. In Sec. II, the classical mechanical and ray-optics formulation of the dynamics of particles and trajectories of light in a $1/r$-"potential" are presented. In Sec. III, the analytical solution for the ray-optics case is derived. In Sec. IV, analogies of the ray-optics solution are explored with respect to the classical Rutherford scattering problem and an experimental demonstration is given in Sec. V. In Sec. VI, the wave-mechanical pictures are explored. The correspondence between quantum mechanical (QM) Coulomb scattering and the scalar electric field in the refractive index field is revealed. Thereafter, the correspondence to the classical ray picture in the latter case is established via QM wave-packet scattering, finally recovering the photonic Rutherford trajectory presented in Sec. IV.

II. CLASSICAL LIMIT: FERMAT'S PRINCIPLE

A differential equation suitable for both massive particles and light is obtained via a variational principle, with fixed-path endpoints, that unifies Maupertius' (mechanics) and Fermat's (optics) variational principles:[4,5]

$$\frac{d^2\mathbf{r}}{ds^2} = \nabla\left(\frac{1}{2}n^4(\mathbf{r})v^2(\mathbf{r})\right), \quad \left|\frac{d\mathbf{r}}{ds}\right| = n^2(\mathbf{r})v(\mathbf{r}). \tag{1}$$

Here $\mathbf{r}$ is a vector denoting a point on the path and s is a stepping parameter that increases along the path. The difference in treating light or massive particles rests in the proper choice of the velocity $v(\mathbf{r})$ and the parameter s.

For massive particles one can take $n = 1$ such that Eq. (1) reduces to Newton's second law. The usual classical dynamics are obtained with the choice of the stepping parameter $ds = dt$, by setting $v^2/2 = E/m - V/m$, the difference between the total and potential energy per unit mass.[5] Equation (1) can even be used to describe relativistic gravitational mechanics of massive particles in a static space-time metric by an appropriate non-unit refractive index.[4,5]

To describe the paths of light, Eq. (1) is to be supplemented by setting v to the phase velocity of light in matter $v = c/n$, where c is the vacuum speed of light. This case corresponds to Fermat's principle of the least optical path and allows the calculation of light trajectories through a spatially inhomogeneous refractive index field $n(\mathbf{r})$. This picture provides a classical particle picture of light propagation and corresponds to the zero-wavelength limit of wave optics.[6] The result is the "$F = ma$" optics developed by Evans *et al.* and explored by many others.[7–10]

In summary, Eq. (1) takes the following forms for particles and light, respectively:

$$\text{Mechanics}: \quad m\frac{d^2\mathbf{r}}{dt^2} = -\nabla V(\mathbf{r}), \quad \left|\frac{d\mathbf{r}}{dt}\right| = v(\mathbf{r}), \tag{2}$$

$$\text{Optics}: \quad \frac{d^2\mathbf{r}}{ds^2} = \nabla\left(\frac{1}{2}n^2(\mathbf{r})\right), \quad \left|\frac{d\mathbf{r}}{ds}\right| = n(\mathbf{r}). \tag{3}$$

Downloaded 20 May 2013 to 139.18.110.156. Redistribution subject to AAPT license or copyright; see http://ajp.aapt.org/authors/copyright_permission

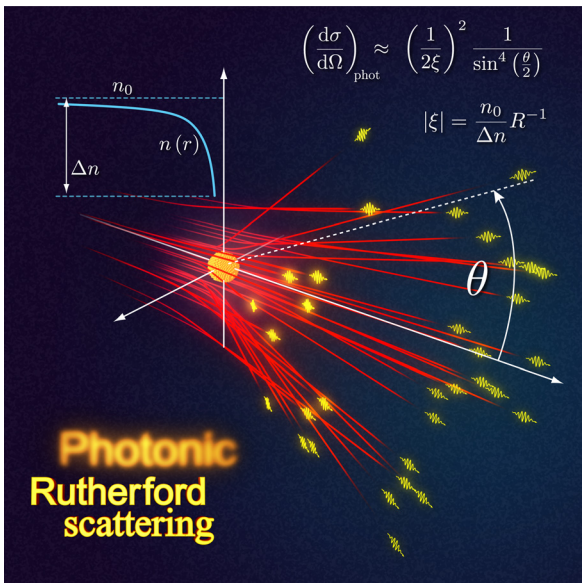

Fig. 1. (Color online) Artist's rendering of photonic wave packet scattering by a thermal lens $n(r)$ [Eq. (5)] around a hot nanoparticle.

The solution to Eq. (2) for a $1/r$ potential is best known from Kepler's problem or Rutherford scattering (see Sec. IV).

While a rather artificial type of refractive index field $n^2(r) = \text{const.} + \text{const.}/r$ has been shown to yield all types of Kepler orbits for light,[5,9] we will now seek a more physical and common analogy in the optical domain. For this, consider a point-like heat source that generates a temperature profile $T(\mathbf{r}) = T_0 + \Delta T(r)$ in the surrounding medium with

$$\Delta T(r) = \frac{Q}{4\pi\kappa r}, \tag{4}$$

which, according to Fourier's law, decays with the inverse distance r from the object to T_0 at infinite distance (Q and κ are the heat-source power and the medium heat conductivity, respectively).[11,12] This temperature profile results in a refractive index profile that takes up the inverse distance dependence with the thermo-refractive coefficient dn/dT as a proportionality factor

$$n(\mathbf{r}) = n_0 + \frac{dn}{dT}\Delta T(\mathbf{r}) = n_0 + \Delta n\frac{R}{r}, \tag{5}$$

where $n_0 = n(T_0)$ is the unperturbed real-valued refractive index, R is the radius of the heat-source, and $\Delta n = \Delta T(R)\, dn/dT$ is a real-valued refractive index contrast. With the thermo-refractive coefficient dn/dT being a material parameter and a given heat-source power Q, the contrast Δn is determined and characterizes a specific experimental situation. This scenario is to a good approximation realized for the steady state of an individual spherical embedded heat source outside the sphere at $r > R$. As we will demonstrate, the problem of finding the ray trajectories fulfilling Eq. (3) is closely related to the scattering by an unshielded Coulomb potential (i.e., Rutherford scattering).

III. EXACT SOLUTION

Because (by symmetry) the trajectories are confined within a plane (see Fig. 2), cylindrical coordinates $\{r, \phi\}$ with the corresponding expressions for acceleration and gradient are appropriate. A prime ($'$) will denote differentiation with respect to the stepping parameter s. Fermat's least optical path principle [Eq. (3)] then gives two equations for the radial and angular coordinates

$$\hat{\mathbf{r}}: \quad r'' - r\phi'^2 = \underbrace{-n_0\Delta nR\frac{1}{r^2}}_{\text{attractive/repulsive}} \underbrace{-\Delta n^2R^2\frac{1}{r^3}}_{\text{attractive}}, \tag{6}$$

$$\hat{\theta}: \quad r\phi'' + 2r'\phi' = 0. \tag{7}$$

This set of coupled differential equations is equivalent to the perturbed Kepler problem with its precessing orbit solutions.[13] Equation (7) yields the conserved optical angular momentum $L_z = r^2\phi' = bn_0$, that is, $L_z' = 0$.[7] The parameter $b > 0$, the so-called impact parameter, is the distance of the approaching parallel ray to the optical axis [see Fig. 2(a)]. Equation (6) involves the analogue to the mechanical radial force terms and shows a $1/r^2$ interaction, which is either attractive or repulsive depending on the sign of Δn, and a perturbation by a $1/r^3$ term, which is always attractive.

We now introduce the constant

$$\xi = -\frac{n_0}{\Delta nR}, \tag{8}$$

which is a measure of the inverse strength of the heat-induced refractive index gradient and encodes the polarity of the interaction in such a way that a positive sign of ξ corresponds to repulsion. Equation (6) can be recast in the usual manner into an equation for $u = 1/r$ (e.g., from Binet's orbit equation,[13] or see Chapter 3.5 in Ref. 14) using conservation of angular momentum to get

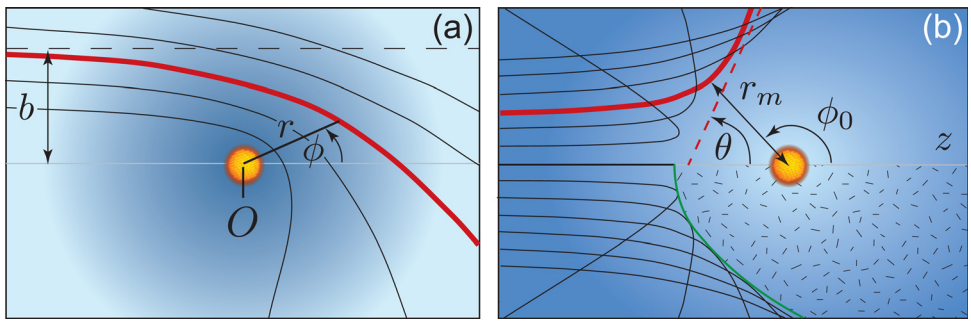

Fig. 2. (Color online) Annotated sketch of a typical ray trajectory (thick line) $r(\phi)$ [Eq. (10)] through the refractive index fields $n(r)$ [Eq. (5)] with (a) $\Delta n > 0$ (attractive) and (b) $\Delta n < 0$ (repulsive).

Downloaded 20 May 2013 to 139.18.110.156. Redistribution subject to AAPT license or copyright; see http://ajp.aapt.org/authors/copyright_permission

$$\frac{d^2u}{d\phi^2} + u[1 - b^{-2}\xi^{-2}] = -\xi^{-1}b^{-2}. \tag{9}$$

If the refractive index in the medium is homogeneous (i.e., $\xi = \infty$), the familiar harmonic oscillator differential equation with unit angular frequency emerges and the solution is $u = b^{-1}\sin(\phi)$, which, in Cartesian coordinates with $y = r\sin(\phi) = b$, is the unperturbed ray [see the dashed line in Fig. 2(a)]. If the profile is present, and requiring for the moment that $|b\xi| > 1$, Eq. (9) has the form of the harmonic oscillator differential equation plus a constant $u'' + c_1 u = -c_2$, with positive c_1. This equation is solved by $u = (c_2/c_1)[e\cos(\sqrt{c_1}(\phi - \phi_0)) - 1]$ with the yet-to-be-determined constants e and ϕ_0. Equation (9) is therefore solved by

$$r(\phi) = \frac{p}{e\cos(\gamma[\phi - \phi_0]) - 1}, \tag{10}$$

where the eccentricity e is allowed to be either positive or negative and with the parameters

$$p = [b^2\xi^2 - 1]/\xi,$$
$$\gamma^2 = 1 - b^{-2}\xi^{-2}. \tag{11}$$

Mathematically, the orbits described by Eq. (10) represent perturbed hyperbolic trajectories with the particle being the exterior ($\xi > 0$) or interior ($\xi < 0$) focus[9] (see Fig. 2). The orbits may show peculiar behavior, such as multiply revolving trajectories for $\xi < 0$, when the perturbation parameter γ approaches zero (see Fig. 3) and were already discussed by Darwin (the grandson of Charles Darwin) in the context of relativistic Rutherford scattering of electrons in 1913.[15] Also, somewhat later in 1916, Sommerfeld, in his relativistic corrections to the hydrogen spectra, encountered the bound form of such orbits for the electron.[16–18]

To obtain the eccentricity e we reconsider the particular choice of the stepping parameter in Eq. (3) and write again in cylindrical coordinates

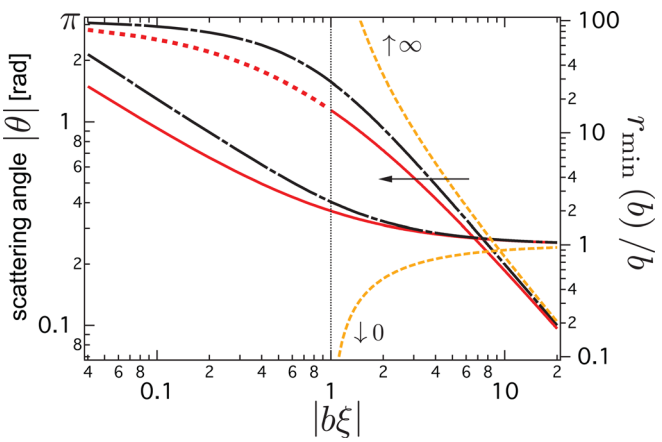

Fig. 3. (Color online) Absolute scattering/deflection angle $|\theta|$ (left axis) and the normalized distance of closest approach $r_{\min}(b)/b$ (right axis) vs. the normalized impact parameter $|b\xi|$ for fixed interaction strength $|\xi^{-1}|$. Black dashed-solid lines: Rutherford scattering; red (or dark gray) lines: exact solution; orange (or light gray) dashed lines: attractive. Clearly visible is the effect of the additional attractive perturbative force allowing closer approaches and weaker deflections for the repulsive case ($\xi > 0$) and stronger deflection in the attractive case ($\xi < 0$). For $b\xi \gg 1$ the results converge—photonic Rutherford scattering is a good approximation to the exact solution.

$$|\mathbf{r}'| = n \;\rightarrow\; r'^2 + r^2\phi'^2 = n(r)^2. \tag{12}$$

The radius of closest approach is found by setting $r' = 0$ and yields $r_m = b + \xi^{-1}$. Comparison of this expression to the corresponding minimum radius as described by Eq. (10), which gives $r_m = p/(e-1)$ at the angle of closest approach $\phi = \phi_0$, yields the eccentricity $e = b\xi$. Setting the denominator of Eq. (10) to zero yields the extreme angles $\theta_\infty^{\pm} = \pm|\gamma^{-1}|\arccos(1/e) + \phi_0$. Requiring that the ray approaches parallel to the optical axis from negative infinity [see Fig. 2(b)], i.e., $\theta_\infty^{+} = \pi$, will orient the solution in Eq. (10) according to the imposed initial conditions. We then also find the angle of closest approach

$$e = b\xi,$$
$$\phi_0 = \pi - |\gamma^{-1}|\arccos(e^{-1}). \tag{13}$$

The parameters in Eqs. (11) and (13), together with Eq. (10), now fully determine the ray trajectory. The scattering angle $\theta = \theta_\infty^-$ (the deflection angle of an incoming horizontal ray)[14] may be expressed as $\theta = 2\phi_0 - \pi$.

The previous treatment relied on the assumption, valid in practical situations, that $|b\xi| > 1$. If the impact parameter gets very small, γ would become imaginary. This peculiarity is formally due to the presence of the attractive inverse-cubic interaction term that dominates the inverse-squared term at small distances [see Eq. (6)]. Instead of Eq. (9) we must then solve the differential equation $u'' - c_1 u = -c_2$ with positive c_1. Its general solution is

$$r_s(\phi) = \frac{p_s}{e_1\exp(\gamma_s\phi) + e_2\exp(-\gamma_s\phi) + 1}, \tag{14}$$

with the positive perturbation parameter determined by $\gamma_s^2 = -\gamma^2$ and parameter $p_s = -p$. This ansatz allows the incoming ray to have the correct distance at infinity [$\lim_{\phi\to\pi}\sin(\phi)\, r_s(\phi) = b$] and gives the set of two generalized eccentricities

$$e_1 = -\exp(-\pi\gamma_s)\left[\frac{p_s + b\gamma_s}{2b\gamma_s}\right],$$
$$e_2 = -\exp(\pi\gamma_s)\left[1 - \frac{p_s + b\gamma_s}{2b\gamma_s}\right]. \tag{15}$$

Solution (14) works for both the attractive and repulsive cases. In the former case, the solution is a mixture of the hyperbolic sine and cosine which describes trajectories approaching from infinity and falling within a finite time into the coordinate origin. It does so without a closest distance r_m. Both phenomena continue the limiting behavior of Eq. (10), where the closest approach distance goes to zero and the scattering angle θ diverges to infinity as $|b\xi| \to 1$, i.e., the rays revolve ever more vigorously around the origin [see the dashed lines in Fig. 3]. In the case of a repulsive interaction the solution given above involves only the hyperbolic cosine, equivalent to Eq. (10) with complex argument (γ) for the cosine. From the exact solution found here we will now formulate a revealing approximation valid for most physical situations, where $|b\xi| = (b/R) \times (n_0/|\Delta n|) \gg 1$.

IV. PHOTONIC RUTHERFORD SCATTERING

As the refractive index change itself is typically small for most materials ($|\Delta n| \approx 10^{-3}$), and since $b > R$ for the

Downloaded 20 May 2013 to 139.18.110.156. Redistribution subject to AAPT license or copyright; see http://ajp.aapt.org/authors/copyright_permission

incoming rays, the product $|b\xi|$ is typically much greater than 1. This allows us to replace Eq. (10) by the solution to Eq. (9) without the attractive perturbation term

$$r(\phi) \approx \frac{|\xi| b^2}{\sqrt{b^2\xi^2 + 1}\cos(\phi - \phi_0) \pm 1}, \tag{16}$$

with $\pm 1 = -\xi/|\xi|$. This is the exact analogue to the classical (non-relativistic) Rutherford scattering solution of Eq. (2) for the potential $V(r) = Cr^{-1}$, given by

$$r_{\mathrm{RF}}(\phi) = \frac{2Eb^2/|C|}{e\cos(\phi - \phi_0) \pm 1}, \tag{17}$$

where an attractive interaction ($C < 0$) is represented by the upper sign and a repulsive interaction ($C > 0$) by the lower sign. The scattered particle trajectory is determined by its total energy $E = mv_0^2/2$ and mass m. The interaction is determined by the Coulomb force constant $C = q_1 q_2/(4\pi\epsilon_0)$ for the two charges $q_{1,2}$ and prescribes the mechanical force $\mathbf{F}(r) = Cr^{-2}\,\hat{\mathbf{r}}$ acting on the scattered particle. The scatterer is assumed to be fixed here, i.e., it has an infinite mass compared to the scattered particle. The positive eccentricity of the orbit is determined by $e^2 = 4E^2b^2C^{-2} + 1$ and the angle of closest approach is $\phi_0 = \pi \pm \arccos(1/e)$. The angular momentum of the particle relative to the scatterer at the origin is $L = mv_0 b$, while its specific angular momentum (twice the areal velocity[14]) is $L_z = L/m$.

The deflection of photons by a weak gradient index lens generated by a heated point-like absorber, described by Eq. (16), is thus the complete photonic analogue of Rutherford scattering of α particles by a single nucleus [Eq. (17)]. One can therefore identify the photonic analogue of the potential energy as $V \to -n(r)^2/2 + n_0^2/2 \approx n_0^2\,\xi^{-1} r^{-1}$, which decays to zero at infinite distance. The total energy in this analogy is $E \to n_0^2/2$ and the equivalent of the Coulomb force constant is $C \to -n_0 \Delta n R$, as can be inferred from Eq. (6). The form of Eq. (3) also requires the mass m to be set to unity in optics.[7] Hence, all further equations—the differential scattering cross section $d\sigma/d\Omega$ with its famous $\sin^{-4}(\theta/2)$ dependence, or the total cross section $\sigma_{>\Theta}$ of scattering by an angle larger than some angle Θ—can be obtained using these equivalences and the substitution $2E/C \to \xi$. The deflection angle θ can thus also be expressed analogously to Rutherford scattering via

$$\cot(\theta/2) = b\xi. \tag{18}$$

The observation that the total energy is positive requires a few comments. Typically,[5,7] it is stated that Eq. (3), $|\mathbf{r}'|^2/2 - n^2/2 = 0$, corresponds to the equation for the total energy analogue, comprised of a kinetic energy term $|\mathbf{r}'|^2/2$ and a potential energy term $-n^2/2$, and thus the total energy in the optical case would be equivalent to the mechanical scenario at zero energy, $E = 0$. However, due to the inclusion of the additional constant shift $(+n_0^2/2)$ of the potential energy scale in V, necessitated by including n_0 in the refractive index profile [Eq. (5)], we find that here the mechanical zero-energy scenario does not represent the optical problem at hand (cf. footnote 15 of Ref. 7). Indeed, the parabolic unit-eccentricity orbits of zero-energy particle scattering are not the found (approximate) solutions for the ray trajectories. Here, $|\mathbf{r}'|^2/2 + V - n_0^2/2 = 0$ and E can be identified with the first two terms, yielding $E = n_0^2/2$ to be taken as the mechanical total-energy analogue. Thus, only the unbound (hyperbolic) trajectories from classical mechanics are attainable for $n_0 \neq 0$, with n_0 being a real number corresponding to a transparent medium.

Also notable is the discrepancy by a factor of 2 between the expression for the distance of closest approach for the family of trajectories r_C from particle scattering and the exact value from Eq. (12), $r_m(0) = \xi^{-1}$ (see Table I). The difference stems from the fact that for $b \to 0$ the validity of the approximation $b\xi \gg 1$ and thus Eq. (16) breaks down. For a repulsive potential Eq. (14) then passes the point of closest approach. The same argument explains the difference between the specific closest distances $r_{\min}(b)$ and $r_m(b)$ for individual trajectories. For the repulsive case ($\Delta n < 0$), Eq. (6) shows an additional attractive inverse radius-cubed interaction resulting in a closer approach. Solving Eq. (12) without such a term yields the photonic $r_{\min}(b)$ value listed in Table I. The exact trajectories will thus penetrate the classical Rutherford shadow region[19,20] given by the paraboloid $r_s = 4\xi^{-1}/(1 - \cos\phi)$. For $b\xi \gg 1$, the two expressions coincide and the GOA shadow region behind a typical thermal lens may thereby be determined.

V. EXPERIMENTAL DEMONSTRATION

Rutherford scattering is generally considered for many scattered particles on many nuclei with random impact parameters. Thus, the measurable cross section delivers the same results for attractive or repulsive Coulomb interactions. The photonic equivalent can, however, be tested easily on a single scattering center, even allowing measurement the sign of the interaction (the sign of dn/dT). For this purpose, a macroscopic experiment with a metal sphere embedded in a transparent resin as shown in Fig. 4(a) can be used. Upon heating of the central sphere by a high-power laser, one can measure the direction and magnitude of the deflection of paraxial thin laser beams according to Eq. (18). Using a screen placed at a distance D of a few meters, one may easily observe the deflection $\Delta x \approx D\tan(n_0\theta)$ on the screen. Figure 4(b) shows the result of such a measurement. The probing beam has been focused by a lens with focal length 0.5 m,

Table I. Corresponding expressions in photonic and massive-particle Rutherford scattering.

Quantity	Photonic	Particle
$v(\mathbf{r})$	$n(\mathbf{r})$	$v(\mathbf{r})$
$V(r)$	Cr^{-1}	Cr^{-1}
C	$-n_0 R\Delta n = n_0^2\,\xi^{-1}$	$q_1 q_2/(4\pi\epsilon_0)$
L	$n_0 b$	$mv_0 b$
E	$n_0^2/2$	$mv_0^2/2$
r_C	$2\xi^{-1}$	C/E
$r_{\min}(b)$	$\frac{1}{\xi}\left(1 + \sqrt{b^2\xi^2 + 1}\right)$	$\frac{r_C}{2}\left(1 + \sqrt{4b^2 r_C^{-2} + 1}\right)$
$r_s(\phi)$	$\frac{4\xi^{-1}}{1 - \cos\phi}$	$\frac{2C/E}{1 - \cos\phi}$
$\cot\left(\frac{\theta}{2}\right)$	$b\xi$	$2Eb/C$
$\sigma_{>\Theta}$	$\frac{\pi}{\xi^2}\left[\frac{1 + \cos\Theta}{1 - \cos\Theta}\right]$	$\pi\left(\frac{C}{2E}\right)^2\left[\frac{1 + \cos\Theta}{1 - \cos\Theta}\right]$
$\frac{d\sigma}{d\Omega}$	$\left(\frac{1}{2\xi}\right)^2 \sin^{-4}(\theta/2)$	$\left(\frac{C}{4E}\right)^2 \sin^{-4}(\theta/2)$

Downloaded 20 May 2013 to 139.18.110.156. Redistribution subject to AAPT license or copyright; see http://ajp.aapt.org/authors/copyright_permission

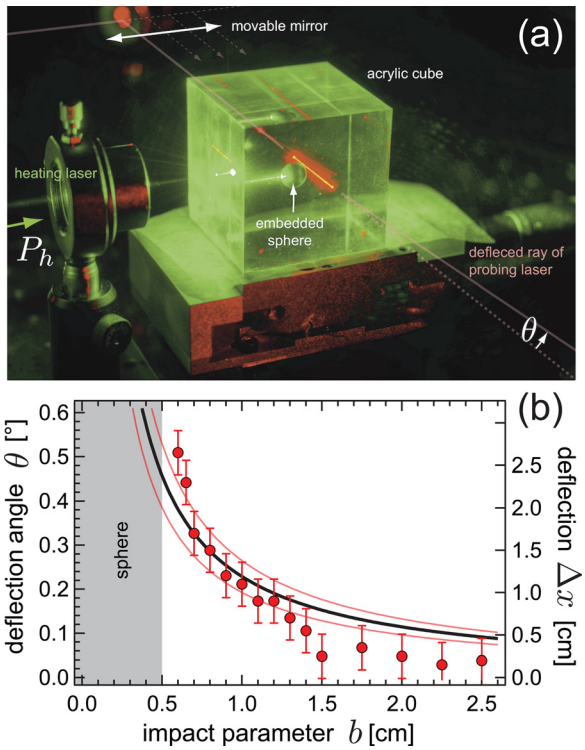

Fig. 4. (Color online) Macroscopic experiment on a single Rutherford-like photonic scatterer. A sphere of radius $R = 0.5$ cm (with a small hole to enhance absorption efficiency) is embedded in an acrylic block (PMMA, 65-mm cube) with material properties $\kappa \approx 0.2\,\mathrm{Wm^{-1}K^{-1}}$, $dn/dT \approx -1.15 \times 10^{-4}\,\mathrm{K^{-1}}$, and $n_0 = 1.49$. The plot shows the results of an experiment with $D = 2.98$ m. The heating laser power was $P_h = 0.8$ W, giving a temperature estimate [Eq. (4)] of $\Delta T(R) \approx 64$ K. A fit of the data (solid line and 2σ confidence band) with Eq. (18) gives $\xi = (501 \pm 80)\mathrm{cm^{-1}}$ and thereby $\Delta T(R) = (52 \pm 8)$K, revealing probably additional convective heat transport. The error bars were estimated using a read-off accuracy of the laser spot's center of intensity. The remaining systematic deviation is likely due to the single-mold manufacturing process.

producing a very fine beam. The offset b of this beam was controlled by a 45° movable mirror as seen in Fig. 4(a). Alternatively, the GOA shadow region behind such a specimen can be observed for a broad and parallel illumination.

The photonic Rutherford scattering can be seen directly with the unaided eye. This could also be quantified to check the deflection-to-impact parameter relation Eq. (18) via image processing. Viewing an object through such a medium containing a heat point source will cause the viewed object to appear warped according to the extrapolated paths as shown in Fig. 5.

Yet another nice physical effect can be demonstrated with such an object. A refractive index profile of $n(r) = 1 + 2GMc^{-2}r^{-1}$ describes gravitational lensing—the path of light in gravitational fields as predicted by Einstein's theory of general relativity.[4,5,9,21–23] Therefore, the observed distortion nicely models, for instance, the famous Einstein ring phenomenon if a material with $\Delta n > 0$ is used. Some types of glasses, such as Schott N-PK51, have this property.[24] While it has proven rather tricky to embed a sphere inside a homogeneous transparent body by hardening resin,[25] it is a feasible student project to create a proper specimen for a deflection experiment by cutting a glass or acrylic cube in half and drilling appropriate semi-spherical exclusions for later reassembly with a fitting sphere inside.

A computer program for interactively visualizing these effects is available in the online supplement to this article.[26] The program can acquaint students with the theoretical

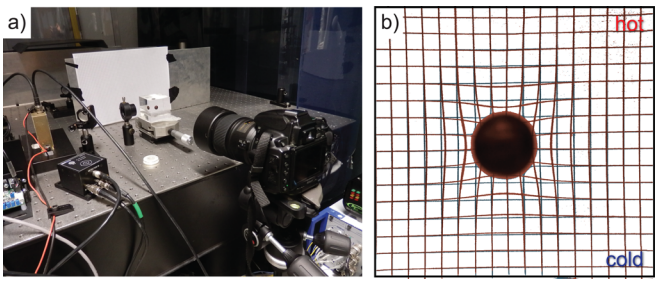

Fig. 5. (Color online) (a) Camera setup to for the photonic scatterer. The laser-heated metal sphere in transparent resin is placed 18 cm in front of a square lattice pattern (lattice constant 0.43 mm). (b) The square pattern photographed through the medium appears warped by the thermal lens. The deflection of rays by the photonic $1/r$ potential gives the illusion of a crunching of the original image photographed before the heating process (darker lines) (enhanced online) [URL: http://dx.doi.org/10.1119/1.4798259.1].

trajectory phenomenology and image distortion effects associated with such a properly heated specimen.

In current research, photothermal single particle microscopy provides measurements on single photonic Rutherford scatterers.[27,28] A simple formalism starting from the ray optics results presented here may be used to provide a semi-quantitative minimal model for photothermal lensing microscopy of heatable metallic nano-particles,[29] a method which has recently reached the sensitivity of single molecules.[30]

VI. WAVE MECHANICAL RUTHERFORD SCATTERING

Both alpha particles and photons obey wave-particle duality. Concepts from scalar wave optics can therefore be applied to quantum particle mechanics, showing the close relation of both. As seen in nuclear scattering experiments,[31,32] molecular interferometry data,[33] or atomic aperture diffraction experiments,[34] interference effects can conveniently be described by Fresnel diffraction.[6,35] The interaction of photons with matter is described by the dielectric function $\epsilon = \sqrt{n}$. This function thus defines a "photonic potential" affecting the propagation of light, which is scalar electric fields in the simplest form of wave optics. While the equivalence of the wave-optics treatment of the spinless Coulomb scattering problem to classical Rutherford scattering in terms of cross sections has been shown,[36,37] we will here showcase the correspondence in optics and use finite width beams to recover the trajectories. To this end, the equivalence between a scalar wave-optics treatment of scattering by the refractive index profile $n(r)$ [Eq. (5)] and the quantum problem of wave-packet scattering on a bare Coulomb potential shall be used.

A. Plane wave scattering

The stationary Schrödinger equation (SE) for scattering by a Coulomb potential reads $H\Psi_C = E\Psi_C$. Here, the Hamiltonian is composed of kinetic and potential energy terms $H = -(\hbar^2/2m)\nabla^2 + C/r$ and the total energy of the unbound scattered particle is $E = \frac{1}{2}mv_0^2$. A wave number k of the incident particle-wave is defined through the de Broglie relation $\hbar k = mv_0$.[38] The time-independent SE can be rewritten as

$$\nabla^2\Psi_C + \left[k^2 - \frac{2\nu k}{r}\right]\Psi_C = 0, \tag{19}$$

Downloaded 20 May 2013 to 139.18.110.156. Redistribution subject to AAPT license or copyright; see http://ajp.aapt.org/authors/copyright_permission

where the interaction parameter $\nu = Ck/2E$ denotes the strength and polarity of the potential, analogous to the force constant C (see Sec. IV). A positive ν corresponds to a repulsive potential and a negative ν to an attractive potential.

The analytical solution was first given by Mott in 1928.[39] A few months later a more elegant form was formulated by Gordon,[36] which can be found by the ansatz $\Psi_C(\mathbf{r}) = e^{ikz}g(r-z)$. The complex-valued function g describes the perturbation of the incoming plane wave and finally transforms Eq. (19) into a soluble differential equation for g. The solution Ψ_C for the case of an incident plane wave reads[38]

$$\Psi_C(\mathbf{r}) = e^{ikz}e^{-\frac{\pi}{2}\nu}\Gamma(1+i\nu)\,{}_1F_1(-i\nu;1;ik[r-z]), \qquad (20)$$

with ${}_1F_1(a;b;z)$ denoting the confluent hypergeometric function and $\Gamma(z)$ being the complex-valued gamma function. The pre-factors ensure a normalization to unity ($|\Psi_C|^2 = 1$) at large distances ($z \to -\infty$) from the scatterer. Equation (20) reduces to the incoming plane wave for vanishing perturbation: $\Psi_C(\mathbf{r}) = e^{ikz}$ for $\nu = 0$. The amplitude of the wave function described by Eq. (20) is shown in Fig. 6.

An asymptotic expansion of the confluent hypergeometric function for $k(r-z) \to \infty$ allows the wave function to be separated into a scattered spherical wave with angle-dependent amplitude f and a plane wave resembling the form $e^{ikz} + f(\theta)e^{ikr}/r$, although both terms will include logarithmic phase distortions due to the long-range character of the Coulomb potential.[38] Apart from corrections vanishing for $r \to \infty$, the scattering cross section reads

$$\frac{d\sigma}{d\Omega} = |f(\theta)|^2 = \left(\frac{\nu}{2k}\right)^2 \frac{1}{\sin^4(\theta/2)}. \qquad (21)$$

Now we will write down the Helmholtz equation for the scalar electric field of light U,[6,35] $\nabla^2 U + k^2[n(\mathbf{r})^2/n_0^2]U = 0$, with the refractive index profile given by Eq. (5). One should think of this equation as being the analogue to the SE with nonzero energy $E = n_0^2/2$ and potential energy $V = -n(\mathbf{r})^2/2 + n_0^2/2$, as in Sec. IV. We find

$$\nabla^2 U + k^2\left[1 + \frac{2\Delta nR}{n_0 r} + \left(\frac{\Delta n^2 R^2}{n_0^2 r^2}\right)\right]U = 0. \qquad (22)$$

A comparison with Eq. (19) shows equivalence to first order in the small quantity $\Delta n/n_0 \ll 1$, and allows identification of the interaction parameter ν as

$$\nu \to -k\frac{\Delta nR}{n_0} = \frac{k}{\xi}. \qquad (23)$$

Arguably, this identification could have been guessed without this inspection simply from the definition of the parameter $\nu = Ck/2E$ and the classical correspondence found earlier with its prescription $2E/C \to \xi$. The solution Ψ_C [Eq. (20)] to the SE of the Coulomb scattering problem can thus be used to find the scalar field amplitude U in the case of scattering of light by the inhomogeneous refractive index field Eq. (5). Identifying U with Ψ_C, the wave-mechanical particle problem can thus be used to obtain results for its corresponding optical phenomenon, similar to the mechanical-optical analogy of Sec. II, which is the "$F = ma$" optics framework. The strength- and polarity-encoding parameter ν is found to be proportional to ξ^{-1} [Eq. (23)] that was the inverse-strength parameter describing the light trajectories.

We have thus demonstrated the equivalence of the plane-wave quantum mechanical Coulomb scattering problem and plane-wave light scattering by our specific thermal lens $n(r)$, with the same approximation used in the correspondence formulated in Sec. IV.

Now let us consider the connection between these wave-mechanical descriptions and the previously studied classical cases. While the shape of the wave function amplitude (Fig. 6) resembles the family of trajectories for a given energy but varying impact parameter [Fig. 2(b)], the resemblance is misleading. For a given constant wavelength λ and thus constant wavenumber, the wave function pattern is only weakly dependent on the strength of the thermal lens (Δn) while the family of trajectories would change significantly. While classical dynamics and scattering descriptions require the notion of paths and trajectories, in the wave-mechanical scattering description no clear correspondence exists for the case of a plane wave.[40] It is only in the far field that the classical average particle number density coincides, up to an additional zero-mean oscillation with an undetectably high spatial frequency, with the quantum wavefunction amplitude[20] and thus with the classical expressions for the cross section $(d\sigma/d\Omega)$. This energy-independent coincidence of classical and spinless quantum-mechanical scattering cross sections,[38] however, is a rather special coincidence[41,42] for the three-dimensional Coulomb problem and would fail in a two-dimensional world.[41] We will therefore now formulate the strict classical limit that connects the wave and classical descriptions.

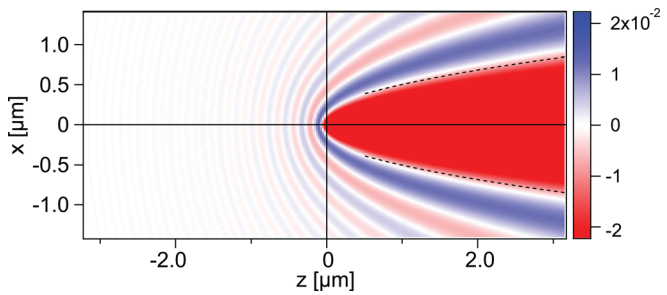

Fig. 6. (Color online) Plane-wave Rutherford scattering. Change in the wave amplitude upon scattering $|\Psi_C^{kz}(x,z)|^2 - 1$, from Eq. (20). The dark shaded bands alternate between positive and negative values. Parameters are $\nu = 0.0214, k = 14.4\,\mu\text{m}^{-1}$. Dashed lines show the interference zone[37] extent $\theta_0 = \sqrt{\pi/kz}$.

B. Wave packet scattering

In order to draw the connection between the classical and wave pictures both in optics and quantum mechanics as we have described above, it is necessary to reconsider what constitutes the classical limit such that a correspondence can be expected. In the previous paragraph, it was shown that the plane wave approach does not resemble the classical picture, apart from the total far-field scattering cross section. In optics, the transition is reached by letting the wavelength λ go to zero.[6] In quantum mechanics, the transition is formally achieved by $\hbar \to 0$ and considering spatially localized wave functions (cf. Ref. 38, Section 6). Due to the possession of the exact solution in scalar wave theory, the transition to the classical trajectories will be outlined in the following. The quantum scattering problem of a wave packet (WP) will be used to this end.

Downloaded 20 May 2013 to 139.18.110.156. Redistribution subject to AAPT license or copyright; see http://ajp.aapt.org/authors/copyright_permission

Following Baryshevskii *et al.*[37] and similar works,[43,44] one can express an initial wave packet localized near (i.e., a light-beam focused at) $\mathbf{r_0}$ at time $t=0$ as

$$U_0^{\mathrm{wp}}(\mathbf{r},0)=\int d\mathbf{k}\,A(\mathbf{k})e^{i\mathbf{k}\cdot(\mathbf{r}-\mathbf{r_0})}. \tag{24}$$

The plane-wave spectrum $A(\mathbf{k})$ defines the WP form in space. For different momenta $\mathbf{k}$, and thus possibly different interaction parameters $\nu_k=kC/2E$ or $\nu_k=k\xi^{-1}$, the solution formerly written down for $\mathbf{k}=k\,\hat{\mathbf{z}}$ [Eq. (20)] can be given in a fixed coordinate frame for an arbitrary direction of the incident wave vector as

$$U_C^{\mathbf{k}}(\mathbf{r})=e^{-\pi\nu_k/2}e^{i\mathbf{k}\cdot\mathbf{r}}\,\Gamma(1+i\nu_k)_1F_1(-i\nu_k;1;i[kr-\mathbf{k}\cdot\mathbf{r}]). \tag{25}$$

The time evolution of an arbitrary initial WP as described by Eq. (24) can then be written as the superposition U_C^{wp} of the individual plane wave solutions corresponding to the plane wave spectrum components of this WP

$$U_C^{\mathrm{wp}}(\mathbf{r},t)=\int d\mathbf{k}\,A(\mathbf{k})e^{-i\mathbf{k}\cdot\mathbf{r_0}}\,U_C^{\mathbf{k}}(\mathbf{r})e^{-i\omega_k t}, \tag{26}$$

where $\omega_k=\hbar k^2/2m$ for matter WPs and $\omega_k=ck$ for light pulses.[44]

Now, two approaches would yield the classical trajectories. A WP describing a massive particle localized in all three spatial directions having a certain frequency width $\Delta\omega\propto\Delta k^2$ would have a corresponding spatial width $\Delta x\propto 1/\Delta k$ whose time evolution of its probability amplitude $|\Psi_C^{\mathrm{wp}}(\mathrm{r},t)|^2$ would trace the dynamics predicted by classical Rutherford scattering, i.e., would follow $r(t)$.[43] Because we can also interpret Eq. (26) to give the optical scalar field U_C^{wp}, we can recover the classical (ray) optics limit by considering $k\to\infty$ and constant energy $\Delta E\propto\Delta k=0$. Assuming non-constant energy would yield a light pulse of duration $\Delta t\propto 1/\Delta E$. Confining the WP in two dimensions and assuming that only different incident angles will contribute, i.e. having a constant wavelength λ and thus constant wave vector $|\mathbf{k}|=\bar{k}=n2\pi/\lambda$, a static limit of ray optics with a well-defined impact parameter is achieved. Further, we will consider an azimuthally symmetric angle distribution for the wave vector spectrum.

More specifically, we will choose a polar angle spectrum to be a Gaussian with an angular width of σ_ϑ, such that it takes the form

$$A(\mathbf{k})=A(k,\vartheta,\varphi)=\delta(\bar{k}-k)\exp(-\vartheta^2/2\sigma_\vartheta^2), \tag{27}$$

where the wave vector has been expressed in spherical coordinates. This results in a focused (non-normalized) WP which has similar properties to the TEM_{00}-mode Gaussian beam[35] with a characteristic width scale given by $\omega_\vartheta=2/(k\sigma_\vartheta)$ (see Fig. 7). In fact, as is the case for the beam emerging from a laser pointer, its lateral intensity follows closely a Gaussian distribution of width ω_0: $|\Psi_0^{\mathrm{wp}}(x)|^2\propto\exp(-2x^2/\omega_0^2)$, while the axial intensity pattern is enveloped by a Lorentzian profile with a corresponding Rayleigh range $z_R=k\omega_0^2/2$: $|\Psi_0^{\mathrm{wp}}(z)|^2\propto 1/(1+z^2/z_R^2)$. Specifically, fitting reveals the relation $\omega_0\approx 0.8\,\omega_\vartheta$, which is expected for the specific angular spectrum representation chosen for the beam.[45]

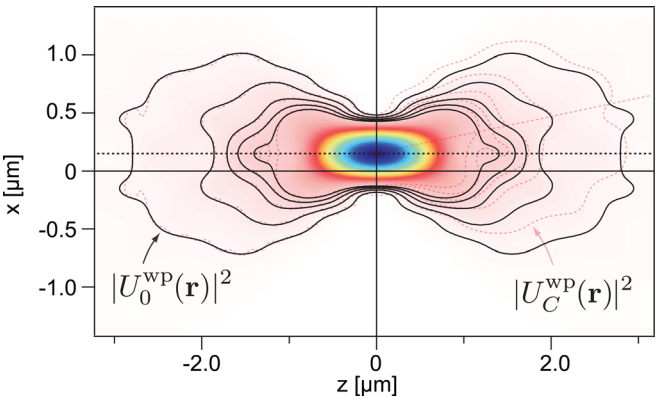

Fig. 7. (Color online) Initial wavepacket $U_0^{\mathrm{wp}}(\mathbf{r})$ [Eq. (24)] (image and solid contours) and scattered wave packet $U_C^{\mathrm{wp}}(\mathbf{r})$ [Eq. (28)] (dashed contours). The parameters were $\nu=0.17, k=14.4\,\mu\mathrm{m}^{-1}, \mathbf{r_0}=(150\,\mathrm{nm})\hat{\mathbf{x}}, \sigma_\vartheta=27.7^\circ$, with corresponding width scale $\omega_\vartheta=0.286\,\mu$m and a Gaussian beam waist of $\omega_0=0.256\,\mu$m.

The solution to the time-dependent SE [Eq. (26)] with the specific choice of the initial WP as described by Eq.(27), then reads

$$U_C^{\mathrm{wp}}(\mathrm{r},t)=\int_0^\pi d\vartheta\int_0^{2\pi}d\varphi\sin(\vartheta)A(\vartheta)e^{-i\mathbf{k}\cdot\mathbf{r_0}}e^{-\pi\nu/2}e^{i\mathbf{k}\cdot\mathbf{r}}\times\Gamma(1+i\nu)_1F_1(-i\nu;1;i[\bar{k}r-\mathbf{k}\cdot\mathbf{r}])e^{-i\hbar\bar{k}^2t/2m}, \tag{28}$$

with $\nu_k=\nu$ and the dot product of the wave vector with the radius vector in spherical coordinates $\mathbf{k}\cdot\mathbf{r}=\bar{k}r[\cos\theta\cos\vartheta+\sin\theta\sin\vartheta\cos(\phi-\varphi)]$.

To obtain the ray limit, we first note that the angular spreading of the WP decreases—becomes paraxial and resembling a ray—when the wavelength decreases, since $\sigma_\vartheta\propto\lambda/\omega_\vartheta$. We then choose beams of a finite width ω_ϑ and small angular spread (i.e., paraxial) with a lateral offset in the x-direction of the resulting stretched WP to some $x_0\gg\omega_\vartheta$. In this case, one must set $\mathbf{k}\cdot\mathbf{r_0}=\bar{k}\,x_0\sin(\vartheta)\cos(\pi-\varphi)$. We then find the WPs to be distorted by the scattering process such that the probability amplitude $|U_C^{\mathrm{wp}}(\mathrm{r})|^2$ follows the classical Rutherford scattering trajectory $r(\theta)$ [Eq. (16)] with the plane polar angle ϕ now being the polar angle θ, and the impact parameter set to the initial WP lateral offset $b\to x_0$ and the lens strength parameter $\xi\to\bar{k}/\nu$. This correspondence is shown in Fig. 8 and is the analogue to Fig. 2(b). This, finally, is the expected classical property of the quantum mechanical scattering description as applied to optics.[43]

C. Outlook: Application in photothermal microscopy

The usefulness of this unified approach is illustrated in its application to photothermal (PT) microscopy.[46] For this limit, it is instructive to look at the wave packet spreading modified by the thermal lens [Eq. (5)] when positioned in front or behind it; that is, by setting $\mathbf{k}\cdot\mathbf{r_0}=\bar{k}z_0\cos\vartheta$ and to observe the collimation for $z_0<0$ or beam broadening for $z_0>0$, leading to a positive or negative enhancement of collected intensity in PT transmission microscopy.[27–29,47] In a PT microscopy experiment a focused beam is used to probe the refractive index lens around a heated nanoparticle. For typical setups, the beam waist is usually around $\omega_0=281$ nm and the beam spread is around $\theta_{\mathrm{div}}\approx 28^\circ$.

Downloaded 20 May 2013 to 139.18.110.156. Redistribution subject to AAPT license or copyright; see http://ajp.aapt.org/authors/copyright_permission

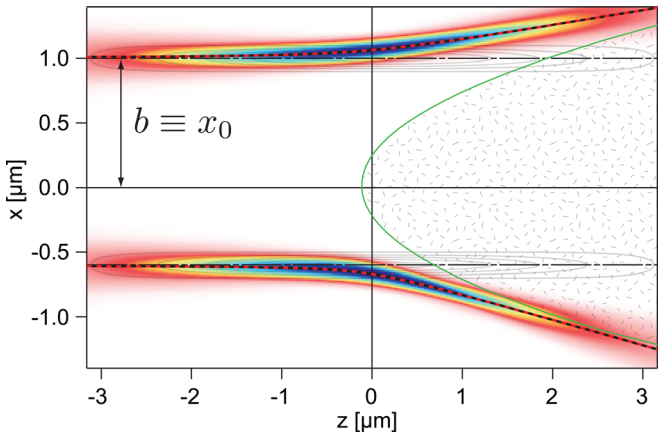

Fig. 8. (Color online) Two different individually scattered/deflected focused beams $|U_C^{\mathrm{wp}}|^2$ [Eq. (28)] positioned at $\mathbf{r_0} = (-0.600\,\mu\mathrm{m})\,\hat{\mathbf{x}}$ and $\mathbf{r_0} = (1.0\,\mu\mathrm{m})\,\hat{\mathbf{x}}$ with a spreading of $\sigma_\vartheta = 3^\circ$ and a corresponding width scale of $\omega_\vartheta = 0.13\,\mu\mathrm{m}$. The strength of the potential was $\nu = 17.1$ and the wave number was $\bar{k} = 289\,\mu\mathrm{m}^{-1}$. The scattered wave packets/beams follow the classical photonic Rutherford trajectories $r(\phi)$ [Eq. (16)] (dashed), similar to Fig. 2(b), and avoid the shadow region (textured area). The contours show the initial wave packet/beam amplitudes $|U_0^{\mathrm{wp}}(\mathbf{r})|^2$ from Eq. (24).

Interestingly, PT single-particle microscopy as described in Refs. 27–29, 46 deals with the interference zone encountered in Sec. VI A (Fig. 6) of plane wave quantum mechanical Coulomb scattering. In this case, the interference zone exhibits a vanishing angular extent $\theta_0 = \pm\sqrt{\pi/kr}$, thus being typically inaccessible and is discarded in scattering analysis thereby leading to the $\sin^{-4}$ dependence of the detectable cross section. In PT microscopy, however, it is widened up to the extent of the angular spread of the plane wave contributions that make up the incident beam (i.e., the angular spread of the probing laser beam). Consequently, the interference zone corresponds to the detected angular domain of PT microscopy and determines the signal. On the other hand, a deflection of the probing beam can be measured and the usual low-energy (wide lateral wave packet width) limit of Rutherford scattering is attained. Deflections of a single scatterer are thus easily optically accessible with a quadrant photodiode.[48]

ACKNOWLEDGMENTS

This work was supported financially by the DFG research unit 877.

[a]Author to whom correspondence should be addressed. Electronic mail: cichos@physik.uni-leipzig.de
[b]Group homepage: http://www.uni-leipzig.de/~physik/mona.html

[1]E. Rutherford, "The scattering of alpha and beta particles by matter and the structure of the atom," Philos. Mag. **21**(125), 669–688 (1911).
[2]H. Geiger and E. Marsden, "On a diffuse reflection of the α-particles," Proc. R. Soc. London, Ser. A **82**(557), 495–500 (1909).
[3]E. R. Wicher, "Elementary Rutherford scattering simulator," Am. J. Phys. **33**(8), 635–636 (1965).
[4]J. Evans, K. K. Nandi, and A. Islam, "The optical-mechanical analogy in general relativity: Exact Newtonian forms for the equations of motion of particles and photons," Gen. Relat. Gravit. **28**(4), 413–439 (1996).
[5]J. Evans, K. K. Nandi, and A. Islam, "The optical-mechanical analogy in general relativity: New methods for the paths of light and of the planets," Am. J. Phys. **64**(11), 1404–1415 (1996).
[6]M. Born and E. Wolf, *Principles of Optics*, 6th ed. (Pergamon Press Ltd., London, 1980).
[7]J. Evans and M. Rosenquist, "'$F = ma$' optics," Am. J. Phys. **54**(10), 876–883 (1986).
[8]J. Evans, "Simple forms for equations of rays in gradient-index lenses," Am. J. Phys. **58**(8), 773–778 (1990).
[9]A. A. Rangwala, V. H. Kulkarni, and A. A. Rindani, "Laplace-Runge-Lenz vector for a light ray trajectory in r^{-1} media," Am. J. Phys. **69**(7), 803–809 (2001).
[10]D. Drosdoff and A. Widom, "Snell's law from an elementary particle viewpoint," Am. J. Phys. **73**(10), 973–975 (2005).
[11]H. S. Carslaw and J. C. Jaeger, *Conduction of Heat in Solids*, 2nd ed. (Oxford U.P., USA, 1986).
[12]The differential equation for heat diffusion around a point heat source Q at the coordinate origin is $Q\delta(\mathbf{r}) = -\kappa\nabla^2 T$, while the electrostatic Coulomb potential V for a point charge q is determined by $\nabla^2 V = -q\delta(\mathbf{r})/\epsilon_0$. These equations are formally identical in structure, such that the temperature field $T(r)$ [Eq. (4)] resembles the Coulomb potential. However, the integration constant for $T(r)$ is the ambient temperature T_0 at infinite distance.
[13]Jean Sivardiere, "Perturbed elliptic motion," Eur. J. Phys. **7**, 283–286 (1986).
[14]H. Goldstein, C. P. Poole, and J. Safko, *Classical Mechanics*, 3rd ed. (Addison-Wesley, San Francisco, 2000).
[15]C. G. Darwin, "XXV. On some orbits of an electron," Philos. Mag. **25**(146), 201–210 (1913).
[16]A. Sommerfeld, "Zur Quantentheorie der Spektrallinien," Ann. Phys. **356**(17), 1–94 (1916); **356**(18), 125–167 (1916).
[17]L. D. Landau and E. M. Lifschitz, *Klassische Feldtheorie*, 8th ed. (Akademie-Verlag Berlin, 1992).
[18]T. H. Boyer, "Unfamiliar trajectories for a relativistic particle in a Kepler or Coulomb potential," Am. J. Phys. **72**(8), 992–997 (2004).
[19]J. W. Adolph, A. L. Garcia, W. G. Harter, G. C. McLaughlin, R. R. Shiffman, and V. G. Surkus, "Some geometrical aspects of classical Coulomb scattering," Am. J. Phys. **40**(12), 1852 (1972).
[20]I. Samengo, R. G. Pregliasco, and R. O. Barrachina, "Classical stationary particle distributions in collision processes," J. Phys. B **32**(8), 1971–1986 (1999).
[21]Fernando de Felice, "On the gravitational field acting as an optical medium," Gen. Relat. Gravit. **2**(4), 347–357 (1971).
[22]S. Deguchi and W. D. Watson, "Diffraction in gravitational lensing for compact objects of low mass," Astrophys. J. **307**(1), 30–37 (1986).
[23]K. K. Nandi and A. Islam, "On the optical mechanical analogy in general relativity," Am. J. Phys. **63**(3), 251–256 (1995).
[24]Schott North America, "Temperature Coefficient of the Refractive Index," Technical Information paper TIE-19 (2008), available online at <http://www.us.schott.com/advanced_optics/english/community/technical-papers-and-tools/tie.html>.
[25]This was professionally done by Realityservice GmbH, Leipzig; see results in Fig. 4.
[26]See supplementary material at http://dx.doi.org/10.1119/1.4798259 for including a simulation program and additional pictures.
[27]M. Selmke, M. Braun, and F. Cichos, "Photothermal single particle microscopy: Detection of a nano-lens," ACS Nano **6**(3), 2741–2749 (2012).
[28]M. Selmke, M. Braun, and F. Cichos, "Nano-lens diffraction around a single heated nano particle," Opt. Express **20**(7), 8055–8070 (2012).
[29]M. Selmke, M. Braun, and F. Cichos, "Gaussian beam photothermal single particle microscopy," J. Opt. Soc. Am. A **29**(10), 2237–2241 (2012).
[30]A. Gaiduk, M. Yorulmaz, P. V. Ruijgrok, and M. Orrit, "Room-temperature detection of a single molecule's absorption by photothermal contrast," Science **330**(6002), 353–356 (2010).
[31]W. E. Frahn, "Fresnel and Fraunhofer diffraction in nuclear processes," Nucl. Phys. **75**(3), 577–591 (1966).
[32]W. E. Frahn, "Diffraction systematics of nuclear and particle scattering," Phys. Rev. Lett. **26**(10), 568–571 (1971).
[33]C. Kurtsiefer, T. Pfau, and J. Mlynek, "Measurement of the Wigner function of an ensemble of helium atoms," Nature **386**(6621), 150–153 (1997).
[34]A. Goussev, "Huygens-Fresnel-Kirchhoff construction for quantum propagators with application to diffraction in space and time," Phys. Rev. A **85**(1), 013626 (2012).
[35]B. E. A. Saleh and M. C. Teich, *Fundamentals of Photonics* (John Wiley and Sons, New York, 1991).
[36]W. Gordon, "Über den Stoss zweier Punktladungen nach der Wellenmechanik," Z. Phys. **48**(3,4), 180–191 (1928).

Downloaded 20 May 2013 to 139.18.110.156. Redistribution subject to AAPT license or copyright; see http://ajp.aapt.org/authors/copyright_permission

[37]V. G. Baryshevskii, I. D. Feranchuk, and P. B. Kats, "Regularization of the Coulomb scattering problem," Phys. Rev. A **70**(5), 052701 (2004).
[38]L. D. Landau and E. M. Lifschitz, *Quantenmechanik*, 8th ed. (Akademie-Verlag, Berlin, 1988).
[39]N. F. Mott, "The solution of the wave equation for the scattering of particles by a Coulombian centre of force," Proc. R. Soc. London, Ser. A **118**(780), 542–549 (1928).
[40]W. Zakowicz, "On the Extincti on Paradox," Acta Phys. Pol., A **101**(3), 369–385 (2002), available at http://przyrbwn.icm.edu.pl/APP/ABSTR/101/a101-3-369.html.
[41]G. Barton, "Rutherford scattering in two dimensions," Am. J. Phys. **51**(5), 420–422 (1983).
[42]D. Yafaev, "On the classical and quantum Coulomb scattering," J. Phys. A: Math. Gen. **30**(19), 6981–6992 (1997).
[43]W. Zakowicz, "Classical properties of quantum scattering," J. Phys. A: Math. Gen. **36**(15), 4445–4464 (2003).
[44]W. Zakowicz, "Scattering of narrow stationary beams and short pulses on spheres," Europhys. Lett. **85**(4), 40001-1–6 (2009).
[45]L. Novotny and B. Hecht, *Principles of Nano-Optics*, Third edition (Cambridge University Press, Cambridge, 2006).
[46]D. Boyer, P. Tamarat, A. Maali, B. Lounis, and M. Orrit, "Photothermal imaging of nanometer-sized metal particles among scatterers," Science **297**(5584), 1160–1163 (2002).
[47]S. Berciaud, D. Lasne, G. Blab, L. Cognet, and B. Lounis, "Photothermal heterodyne imaging of individual metallic nanoparticles: Theory versus experiment," Phys. Rev. B **73**, 045424-1–8 (2006).
[48]M. Selmke and F. Cichos, "Photothermal single particle Rutherford scattering microscopy," Phys. Rev. Lett. **110**, 103901-1–5 (2013).

Model of a windmill

From 1790 until 1880 inventors were required to submit a model of their inventions along with their application to the U. S. Patent Office. This model, submitted by George A. Roland in 1881, consists of a front wheel with a set of twelve vanes. Part of the wheel has received an additional set of four vanes (to demonstrate that his invention could have one or two circles of vanes). The wheel has five supporting wood beams, all connected by a thin wire to the central axle, which put the wheel in motion. When the wheel turns, it transfers its rotational movement into a vertical one, making the bottom inverted-U shaped piece of metal go up and down between a small gear. A big tail vane and a top red wind sensor (to control the rotational movement of the wheel depending on the wind's force) were also added. The model rests on a square wooden base. The novelty consists in the details of the construction and the combination of the several parts of this wind-wheel and its connecting mechanism, producing a very efficient and durable device.

This model is a part of the Susan Mae Eichelberg (Glendening/professional name, glendeningsusan@hotmail.com) collection, which includes over 400 patent models of historical significance. Thispatent model collection is one of the exhibits at The Riverbank Historic House Museum in Cornwall on Hudson, New York. The images and this description are courtesy of the Collection of Historical Scientific Instruments, Department of the History of Science, President and Fellows of Harvard College, where these patent models were exhibited in 2009. See patentmodelmuseum.org and riverbankhistorichousemuseum.org.

Downloaded 20 May 2013 to 139.18.110.156. Redistribution subject to AAPT license or copyright; see http://ajp.aapt.org/authors/copyright_permission